AIP | Journal of Applied Physics

60 keV Ar+-ion induced modification of microstructural, compositional, and vibrational properties of InSb

D. P. Datta, S. K. Garg, B. Satpati, P. K. Sahoo, A. Kanjilal, S. Dhara, D. Kanjilal, and T. Som

Citation: Journal of Applied Physics **116**, 143502 (2014); doi: 10.1063/1.4897537

View online: http://dx.doi.org/10.1063/1.4897537

View Table of Contents: http://scitation.aip.org/content/aip/journal/jap/116/14?ver=pdfcov

Published by the AIP Publishing

Articles you may be interested in

Electrodeposition of InSb branched nanowires: Controlled growth with structurally tailored properties
J. Appl. Phys. **116**, 083506 (2014); 10.1063/1.4893704

Argon-ion-induced formation of nanoporous GaSb layer: Microstructure, infrared luminescence, and vibrational properties
J. Appl. Phys. **116**, 033514 (2014); 10.1063/1.4890608

Amorphization and reduction of thermal conductivity in porous silicon by irradiation with swift heavy ions
J. Appl. Phys. **114**, 014903 (2013); 10.1063/1.4812280

The effect of low-energy-ion irradiation on photoluminescence of porous silicon
J. Appl. Phys. **101**, 026101 (2007); 10.1063/1.2422795

Microstructure and secondary phases in coevaporated CuInS 2 films: Dependence on growth temperature and chemical composition
J. Vac. Sci. Technol. A **19**, 232 (2001); 10.1116/1.1329123

Not all AFMs are created equal
Asylum Research Cypher™ AFMs
There's no other AFM like Cypher
www.AsylumResearch.com/NoOtherAFMLikeIt
OXFORD INSTRUMENTS
The Business of Science®

[This article is copyrighted as indicated in the article. Reuse of AIP content is subject to the terms at: http://scitation.aip.org/termsconditions. Downloaded to] IP: 137.189.170.231 On: Sun, 21 Dec 2014 12:41:22

JOURNAL OF APPLIED PHYSICS **116**, 143502 (2014)

60 keV Ar^+-ion induced modification of microstructural, compositional, and vibrational properties of InSb

D. P. Datta,[1] S. K. Garg,[1] B. Satpati,[2] P. K. Sahoo,[3] A. Kanjilal,[4] S. Dhara,[5] D. Kanjilal,[6] and T. Som[1,a)]
[1]*SUNAG Laboratory, Institute of Physics, Bhubaneswar, Odisha 751005, India*
[2]*Surface Physics and Materials Science Division, Saha Institute of Nuclear Physics, 1/AF Bidhannagar, Kolkata 700064, India*
[3]*School of Physical Sciences, National Institute of Science Education and Research, Bhubaneswar 751005, Odisha, India*
[4]*Department of Physics, Shiv Nadar University, Uttar Pradesh 203207, India*
[5]*Surface and Nanoscience Division, Materials Science Group, Indira Gandhi Centre for Atomic Research, Kalpakkam 603102, India*
[6]*Inter-University Accelerator Centre, Aruna Asaf Ali Marg, New Delhi 110067, India*

(Received 3 September 2014; accepted 29 September 2014; published online 9 October 2014)

Room temperature irradiation of InSb(111) by 60 keV Ar^+-ions at normal (0°) and oblique (60°) angles of incidence led to the formation of nanoporous structure in the high fluence regime of 1×10^{17} to 3×10^{18} ions cm^{-2}. While a porous layer comprising of a network of interconnected nanofibers was generated by normal ion incidence, evolution of plate-like structures was observed for obliquely incident ions. Systematic studies of composition and structure using energy dispersive x-ray spectroscopy, Raman spectroscopy, x-ray photoelectron spectroscopy, Raman mapping, grazing incidence x-ray diffraction, and cross-sectional transmission electron microscopy revealed a high degree of oxidation of the ion-induced microstructures with the presence of In_2O_3 and Sb_2O_3 phases and presence of nanocrystallites within the nanoporous structures. The observed structural evolution was understood in terms of processes driven by ion-induced defect accumulation within InSb. © *2014 AIP Publishing LLC*. [http://dx.doi.org/10.1063/1.4897537]

I. INTRODUCTION

The success of nanotechnology in developing small scale electronic and optoelectronic devices, sensors, or solar cells with highly improved performance relied to a great extent upon the unique properties of semiconductor nanostructures originating from quantum confinement of carriers in low-dimension. III–V semiconductors nanostructures, in particular, are promising for applications in high-speed electronic devices and near to mid-infrared optoelectronic devices due to their low band gap and high carrier mobility.[1–4] Among the III–V semiconductors, InSb attracted special attention because of the lowest band gap (0.17 eV at room temperature (RT)) and high electron mobility of 77 000 cm^2 V^{-1} s^{-1}, making it a promising candidate for developing infrared emitters and detectors as well as low power, high speed electronic devices.[5] Recent studies also indicated possibility of InSb to be used in memory devices.[6] Moreover, the Bohr radius of exciton in InSb is 60 nm,[5] which made it convenient to engineer the band gap of InSb nanostructures for potential applications by tailoring their dimension. For instance, InSb nanowires were used in field effect transistor and sensors.[7,8] As a result, synthesis of InSb nanostructures became a focus of research.[5,9–16] Nanowires of InSb were fabricated by techniques like chemical beam epitaxy,[5] template-based deposition,[9] or self-catalysis based growth.[10] In parallel to such techniques, RT irradiation of InSb by energetic ions was successfully used to fabricate a porous InSb layer comprising of a network of interconnected nanofibers.[11,12] In fact, the advantage of ion-beam technique, such as large scale self-organized synthesis in a single step made it a promising method for nanofabrication. However, the energy of the ion beam in earlier studies was in 1–3 MeV range where a nanofibrous layer was generated for applied fluences in the range of $\sim 10^{14}$–10^{15} ions cm^{-2}.[11,12] On the other hand, in focused ion beam (FIB) based studies, it was observed that normally incident 30 keV Ga^+-ion irradiation to fluences of 10^{16}–10^{17} ions cm^{-2} resulted in gradual development of cone-like nanostructures,[15] instead of nanoporous structure. Moreover, when ion beam was incident at an angle θ to the surface, periodic nanoscale ripple or hillock structures were generated at the fluence of 8×10^{15} ions cm^{-2}.[16] Further, with the increase in applied fluence beyond 10^{16} ions cm^{-2}, the ripple structures evolved into cone-like nanostructures having an In rich apex.[16] Re-deposition of sputtered atoms was assumed to play a key role in the formation of such cone-like nanostructures.[15,16] However, whether a nanoporous structure comprising of nanofibers can be fabricated by normally or obliquely incident medium energy ion irradiation of InSb or not remained an open question. Our recent studies[17,18] on medium energy ion irradiation of GaSb in the high fluence regime (7×10^{16}–3×10^{18} ions cm^{-2}) revealed formation of a porous layer whose microstructure was dependent upon ion incidence angle. Since a vacancy mediated mechanism was invoked for understanding the ion induced porosity development in both of InSb and GaSb,[11,13,17,18] medium energy ion irradiation of InSb in the

---

[a)]Author to whom correspondence should be addressed. Electronic mail: tsom@iopb.res.in

0021-8979/2014/116(14)/143502/10/$30.00

high fluence regime ($>10^{17}$ ions cm^{-2}) might lead to the formation of similar nanostructures.

Radiation damage due to irradiation of medium energy ions to high fluence, in general, is expected to lead to the amorphization of a crystalline semiconductor matrix. However, the nanofiber network generated by MeV energy ion irradiation at low fluences was found to contain nanocrystallites embedded in an amorphous matrix.[12] In addition, the cone-like nanostructures generated by FIB irradiation were also found to be polycrystalline. These observations suggested that the processes leading to the development of porosity or formation of nanostructure might also play a role in the transition of a crystalline matrix to an amorphous one. Regarding the application of InSb nanostructures, although crystalline InSb nanowires were used in device applications,[7,8] quantum confinement effect similar to those observed in crystalline nanostructures was demonstrated for amorphous InSb nanostructures.[19] The crystallinity aspect of the nanostructures developed by irradiation to high fluences is, therefore, of great importance both for understanding the evolution process as well as for the possible technological applications. Moreover, oxide phases of In and Sb could be present in InSb nanostructures due to the reactive natures of both In and Sb, although this aspect was not addressed in earlier studies of ion induced evolution of InSb morphologies.[11–13]

Thus, in order to establish energetic ion irradiation as a useful technique for synthesis of InSb nanostructures, in particular, and synthesis of semiconductor nanostructures in general, it becomes imperative to investigate and understand the evolution of microstructure, composition, and crystallinity of medium energy ion irradiated InSb in the high fluence regime.

In this paper, we showed that a porous InSb layer containing nanofibers forms under 60 keV Ar$^+$-ion irradiation in the high fluence range of 1×10^{17} to 3×10^{18} ions cm^{-2}. We further demonstrated the difference in structural evolution for normal and oblique ion incidences. While a network of interconnected nanofibers evolved for normal ion irradiation, a porous layer containing plate-like structures was formed for irradiation at 60°. The structural evolution was understood in terms of irradiation induced growth of voids due to vacancy agglomeration, subsequent void growth, and interconnection. Our studies further revealed the presence of crystalline phases, in the form of nanocrystallites, in the ion-generated microstructure and high level of oxygen absorption, leading to the formation of In_2O_3 and Sb_2O_3 phases.

II. EXPERIMENTAL

Mirror polished *n*-type (Te-doped) InSb (111) wafers were cut into pieces (1×1 cm^2) and ultrasonically cleaned by using trichloroethylene, acetone, ethanol, and de-ionized water. The samples were irradiated at RT with mass separated ^{40}Ar$^+$-ions of energy 60 keV. In order to understand the role of incident angle of ions (θ) in the evolution of microstructures, InSb samples were irradiated at both normal ($\theta = 0°$) and oblique ($\theta = 60°$) angles of ion incidence. The applied fluence was varied from 1×10^{17} ions cm^{-2} to 3×10^{18} ions cm^{-2}. The ion-induced evolution of microstructure was investigated by using a field emission gun based scanning electron microscope (FEGSEM) (Carl-Zeiss) in both plan-view and cross-sectional geometries. The elemental analysis was carried out in plan-view mode by energy dispersive x-ray spectroscopy (EDS) (Oxford Instruments) attached to the SEM, using a 10 keV electron beam. In addition, surface chemical property was studied by x-ray photoelectron spectroscopy (XPS) (VG Instruments) using Mg-K_α radiation source ($h\nu = 1254$ eV). Micro-Raman (Renishaw) spectra of the irradiated samples were also recorded at RT in a backscattering geometry using the 514.5 nm line of an Ar-ion laser. Raman mapping was performed at RT by using the 514.5 nm line of an Ar-ion laser (inVia, Renishaw) and the data were recorded with the help of an 1800 lines nm^{-1} grating and a thermoelectrically cooled CCD detector. Moreover, grazing-incidence (5°) x-ray diffraction (GIXRD) measurements were carried out (Bruker, D8-Discover), by using the Cu-K_α radiation source ($\lambda = 0.154$ nm), to look for crystalline phases in the irradiated samples. Microstructure of samples, irradiated to the highest fluence at $\theta = 0°$ and 60°, was investigated by cross-sectional transmission electron microscopy (XTEM) using a 300 kV field emission gun based TEM (FEI Tecnai G^2 S-Twin).

III. RESULTS AND DISCUSSION

The plan-view and cross-sectional SEM (XSEM) micrographs in Figs. 1 and 2 demonstrate that a porous microstructure was generated by both normally and obliquely incident Ar$^+$-ions at the lowest fluence (viz. 1×10^{17} ions cm^{-2}). It should be noted that this result is in contrast to earlier observations of cone-like structures or ripple pattern formation (at oblique ion incidence) for medium energy ion irradiation of InSb using FIB.[15,16] Moreover, contrasting nature of structural evolution of irradiated InSb for normal and oblique ion incidences also became clear from the SEM images. Normally incident ion irradiation generated a porous layer comprising of an interconnected network of nanofibers as discernible from Fig. 1(a). The widths of the nanofibers were measured to be ∼10–25 nm range. Plate-like structures were also observed to coexist with the interconnected nanofibers [indicated in Fig. 1(a)]. As the applied fluence was increased, lesser numbers of plate-like structures were observed in the porous layer, with further appearance of interconnected nanofibers. This became evident from the plan-view image shown in Fig. 1(c) corresponding to the highest fluence of 3×10^{18} ions cm^{-2}. The XSEM images provided more insight into the microstructural evolution during ion irradiation. The XSEM image in Fig. 1(b), corresponding to the structure shown in Fig. 1(a), clearly demonstrated the formation of a porous layer of thickness around ∼1 μm containing a network of nanofibers. It should be mentioned here that, at the high ion fluences used in the present study, a variation in thickness of the porous layer was detected in XSEM images taken from different places. Plate-like structures coexisting with nanofibers-network were also observed throughout the porous layer. In fact, some nanofibers were seen to extend from plate-like structures in Fig. 1(b). A further close

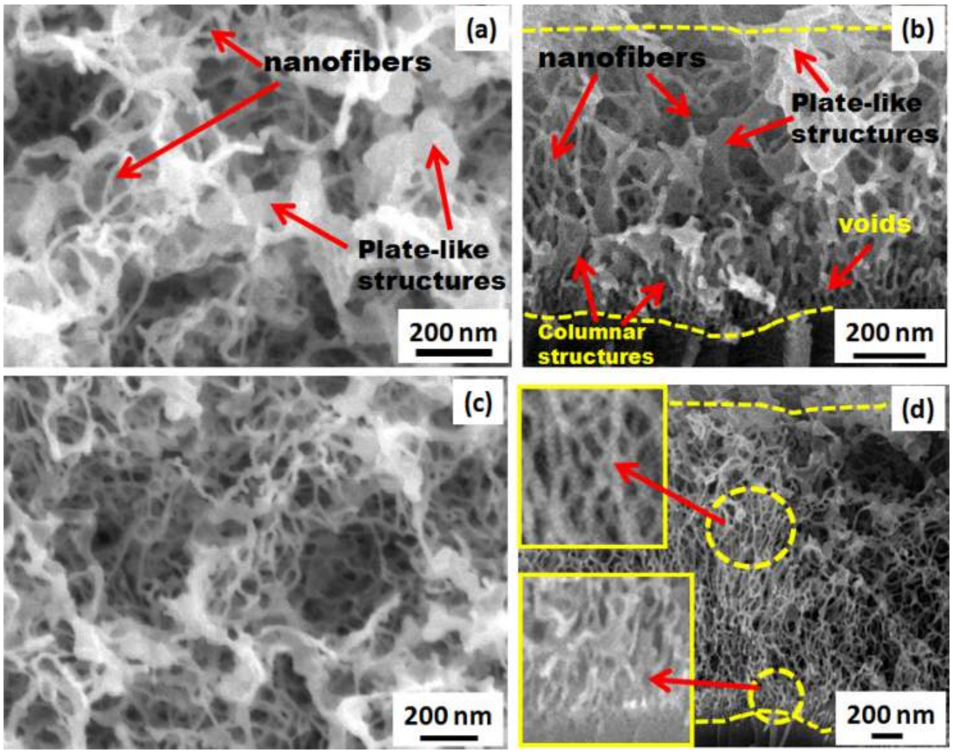

FIG. 1. Plan-view and cross-sectional SEM (XSEM) images of InSb irradiated at $\theta = 0°$, as a function of applied ion fluence. (a) Plan-view; fluence 1×10^{17} ions cm^{-2}, (b) XSEM; fluence 1×10^{17} ions cm^{-2}, (c) plan-view; fluence 3×10^{18} ions cm^{-2}, and (d) XSEM; fluence 3×10^{18} ions cm^{-2}. The dashed yellow lines on the XSEM images show the top surface and the interface with the substrate underneath.

inspection of the interface of the porous layer and the underlying substrate revealed the existence of voids of dimension 20–50 nm along the interface. Columnar structures were observed above the void layer, as indicated in Fig. 1(b). On the other hand, the XSEM image of the sample, irradiated to the highest fluence of 3×10^{18} ions cm^{-2}, in Fig. 1(d) shows that the porous layer mainly comprised of a network of interconnected nanofibers (the inset at the top left corner presents a magnified view). Moreover, an increase in thickness of the porous layer to 1.8–2 μm was observed in Fig. 1(d). The interface region of the porous layer with the underlying substrate, however, showed microstructure similar to the one observed at the lowest fluence [inset at the bottom left corner of Fig. 1(d)]. Here, columnar structures are observed over voids of dimension ~20–50 nm. Thus, normally incident ion irradiation (in this fluence regime) turned out to be an efficient method for fabricating InSb nanofibers.

The porous microstructure formed by irradiation of obliquely incident ions on InSb turned out to be significantly different compared to the ones formed due to normally

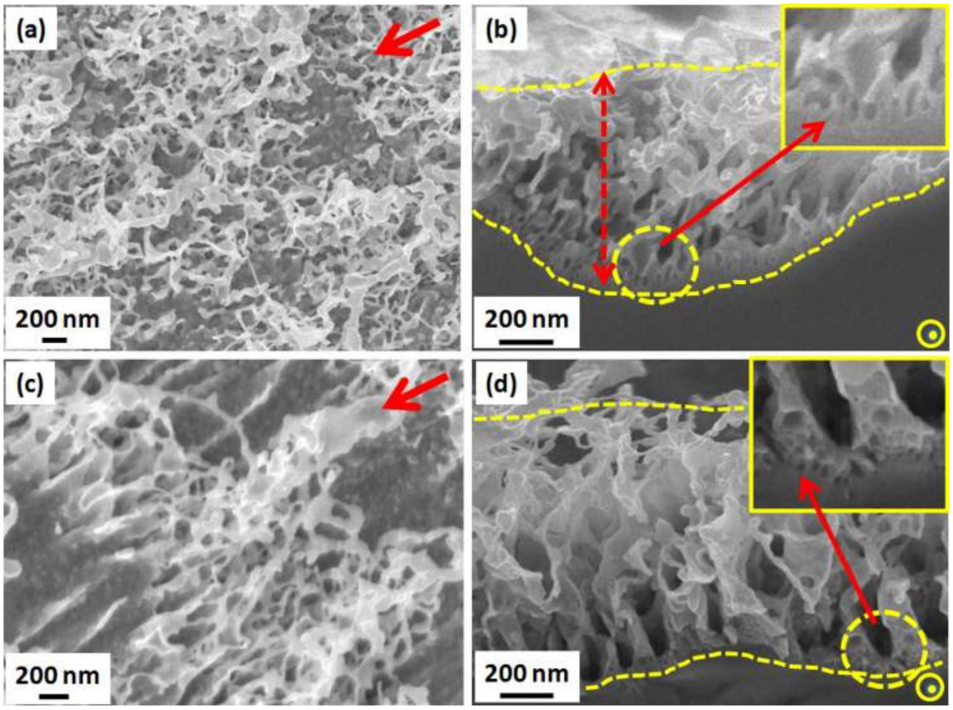

FIG. 2. Plan-view and cross-sectional SEM (XSEM) images of InSb irradiated at $\theta = 60°$, as a function of applied ion fluence. (a) Plan-view; fluence 1×10^{17} ions cm^{-2}, (b) XSEM; fluence 1×10^{17} ions cm^{-2}, (c) plan-view; fluence 3×10^{18} ions cm^{-2}, and (d) XSEM; fluence 3×10^{18} ions cm^{-2}. The XSEM images are taken in a direction perpendicular to the projected ion beam direction depicted by the red arrows on the plan-view images. The dashed yellow lines on the XSEM images show the top surface and the interface with the substrate underneath.

incident ions. The microstructures of InSb samples, irradiated to fluences of 1×10^{17} and 3×10^{18} ions cm^{-2} under oblique ion irradiation, are shown in Figs. 2(a) and 2(b) and Figs. 2(c) and 2(d), respectively. It is clearly seen from the plan-view images of Figs. 2(a) and 2(c) that in contrast to normally incident ions, where porous layer was distributed all over the irradiated surface, obliquely incident ion irradiation resulted in the formation of porous structures in distinct regions on the surface within which the bare irradiated surface was also observed. In fact, the porous regions were arranged in strips over the surface oriented perpendicular to the incident beam direction (depicted by the red arrows on the plan-view images). In the porous regions, plate-like structures were mainly observed with few nanofibers extending from them. Measurements also revealed that widths of plate-like structures are in the range of 15–30 nm, which were slightly higher than those found for normally incident ion-generated structures.

XSEM image shown in Fig. 2(b) illustrates that the plate-like structures were extended from a modulated interface. It should be mentioned here that the XSEM images were taken in a direction perpendicular to the direction of projection of incident ion-beam onto the surface (depicted by the concentric yellow circles on the respective image). In accordance with the plan-view image, the porous layer was found to contain plate-like structures, whereas a few nanofibers extending from the plate-like structures were seen near the top surface. However, the interface of the plate-like structures with the substrate underneath showed the presence of small voids [~20–50 nm wide, also visible in the inset of Fig. 2(b)], similar to the case of normally incident ions. The thickness of the porous layer [from a valley to top, as shown in Fig. 2(b)] was around 700 nm. Within the range of fluence under consideration, obliquely incident ion irradiation showed such porous layer in regions with bare surface in between them. When the ion fluence was increased to 3×10^{18} ions cm^{-2}, the porous layer comprised of similar plate-like structures (of comparable widths), as observed for the lowest fluence, although the thickness of the porous layer increased to ~1 μm [Fig. 2(d)]. In addition, a layer of small voids was also detected at the interface of the porous layer with the substrate underneath (inset in the bottom right corner of Fig. 2(d) presents a magnified view).

EDS analyses revealed that the difference in porous microstructures generated by normally and obliquely incident ion beam had significant influence on their composition. Fluence-dependent compositional variations of the porous structures are displayed in Figs. 3(a) and 3(b) for $\theta = 0°$ and 60°, respectively. Throughout the fluence range of the present study, the concentration of In in the ion irradiated samples remained slightly above Sb for both $\theta = 0°$ and 60°. Moreover, adsorption of O in the microstructure was detected by EDS. For $\theta = 0°$, an increasing trend in the O concentration is discernible in Fig. 3(a). In fact, the amount of O increased from 29% to 35% as the applied fluence was varied from 1×10^{17} to 3×10^{18} ions cm^{-2}, which was accompanied by a slight decrease in the concentrations of In and Sb. In contrast, the concentration of O within the porous structure remained within 12%–13% throughout the fluence range for $\theta = 60°$, except a small enhancement at 1×10^{18} ions cm^{-2}. Since the O adsorption is directly dependent upon the surface area of the structures exposed to ambience, the difference in O concentration in porous layers for $\theta = 0°$ and 60° seemed to be originating from variation in effective surface area of the nanostructures.

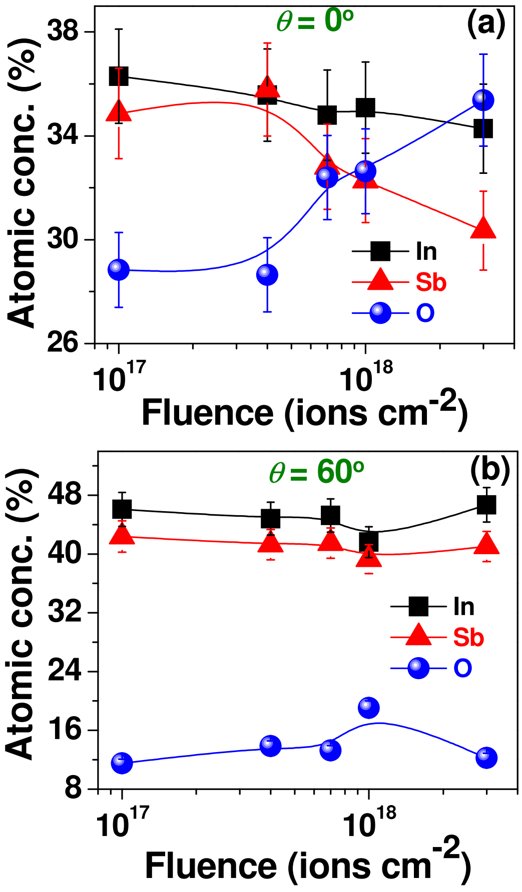

FIG. 3. Atomic concentrations, obtained from EDS analyses, of In, Sb, and O as a function of ion fluence for (a) $\theta = 0°$ and (b) $\theta = 60°$.

Micro-Raman spectroscopic measurements were carried out to detect the possible presence of oxides in the nanoporous layer. The Raman spectra of the samples are shown in Figs. 4(a) and 4(b) for $\theta = 0°$ and 60°, respectively. Indeed, a peak was discernible around 260 cm^{-1} in all the Raman spectra of Figs. 4(a) and 4(b), which could be assigned to Sb_2O_3.[20] In addition, a prominent peak at 178 cm^{-1}, corresponding to TO mode of InSb,[21,22] was observed in the Raman spectra of samples irradiated at $\theta = 60°$ [Fig. 4(b)]. Moreover, a small peak around 157 cm^{-1} was discernible in Fig. 4(b), which was earlier observed by Seok *et al.* for Ar-ion beam etched InSb and attributed to amorphous InSb.[23] On the other hand, although the presence of any peak corresponding to TO mode of InSb or amorphous InSb was not apparent in Fig. 4(a), deconvolution of spectra corresponding to normally irradiated samples (in the region 120–220 cm^{-1}) showed the presence of two peaks at 178 cm^{-1} and 157 cm^{-1}, respectively. While the amorphization of InSb matrix in the present experiment, due to Ar^+-ion irradiation, became apparent from the peak observed at 157 cm^{-1}, the peak corresponding to TO mode of InSb indicated the

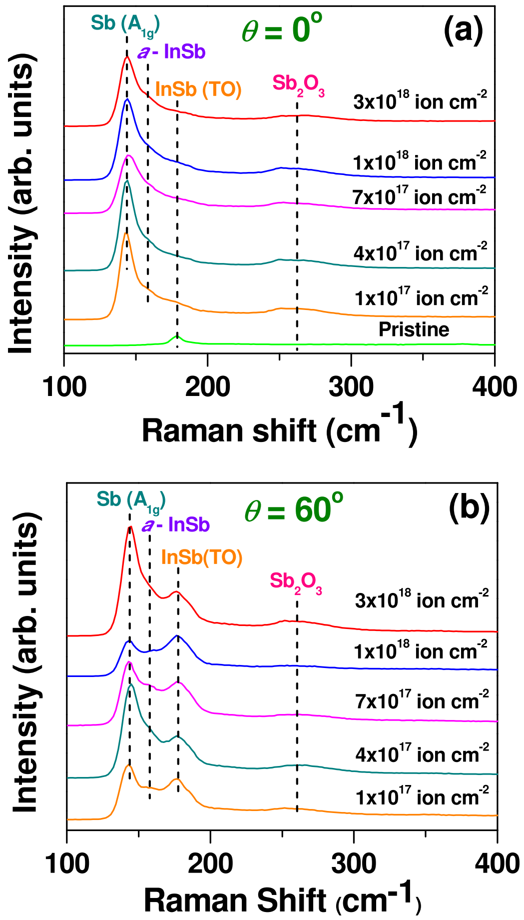

FIG. 4. Micro-Raman spectra of irradiated InSb samples for (a) $\theta = 0°$ and (b) $\theta = 60°$. The spectra are shifted along the *y*-direction for clarity.

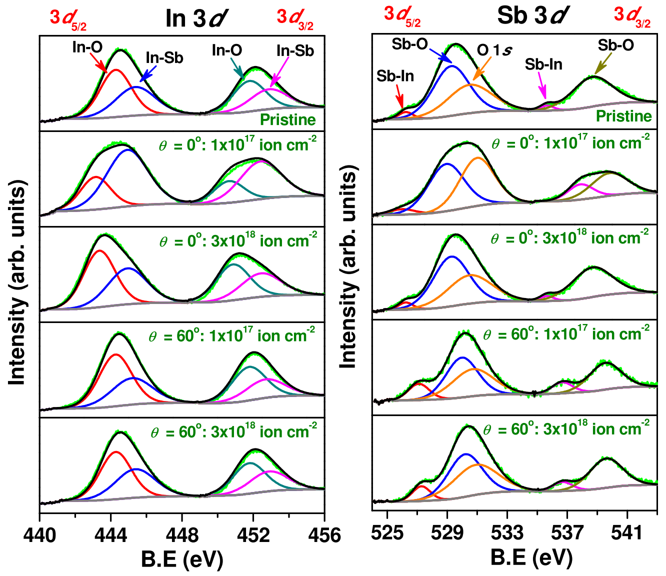

FIG. 5. In 3*d* and Sb 3*d* core level XPS spectra corresponding to the pristine InSb and after irradiation to fluences of 1×10^{17} and 3×10^{18} ions cm^{-2} at $\theta = 0°$ and 60°. The corresponding microstructures are shown in the SEM images of Figs. 1 and 2. Colors refer to collected spectra (light green), fitted curve (black), background (gray), $3d_{5/2}$ component of In-O bond (red) and In-Sb bond (blue), $3d_{3/2}$ component of In-O bond (cyan) and In-Sb bond (magenta), $3d_{5/2}$ component of Sb-In bond (red) and Sb-O bond (blue), $3d_{3/2}$ component of Sb-In bond (magenta), Sb-O bond (dark yellow), and O1*s* bond (orange), respectively.

presence of crystalline phase in the form of nanocrystallites in the porous microstructure. In addition, the peak at 144 cm^{-1} in the Raman spectra of all the irradiated samples matched with the A_{1g} peak of elemental Sb.[24–26] The presence of elemental Sb was correlated with the oxidation of irradiated porous structures and is discussed below.

Since the oxide phase of Sb was detected in Raman spectroscopic studies, XPS measurements were carried out for a detailed analysis of the chemical states present on the surface of the nanoporous structures and evolution of the same with ion fluence. In Fig. 5, we show the recorded spectra of In 3*d* and Sb 3*d* regions for the pristine InSb along with those from InSb samples irradiated to the fluences of 1×10^{17} and 3×10^{18} ions cm^{-2} at 0° and 60°, respectively. Analysis of data showed the presence of oxygen on the pristine sample, indicating the existence of a native oxide layer. In fact, an average thickness of the native oxide layer present on InSb surface was estimated to be ~2 nm in an earlier study.[27] The In 3*d* core level spectra were deconvoluted into In-Sb bonds in InSb (444.3 eV) and In-O bonds in In_2O_3 (445.2 eV) with a spin orbit splitting of 7.5 eV.[27–31] Corresponding Sb 3*d* spectra were deconvoluted into Sb-In bond in InSb (527.4 eV), Sb-O bond in Sb_2O_3 (530.2 eV) with a spin orbit splitting of 9.5 eV.[27–30] The Sb 3*d* spectra further contained O1*s* signal at 531 eV.[27–30] XPS measurements showed the presence of both In_2O_3 and Sb_2O_3 phases in the porous microstructures. The relative amount of the components, determined from XPS data, is shown in Table I. Both for $\theta = 0°$ and 60°, an increasing amount of In corresponding to InSb phase, with ion fluence, was found (Table I), in comparison to that of Sb in InSb phase. This indicates the higher reactivity of Sb with O compared to In, which is discussed below. Also, the relative amount of Sb in Sb_2O_3 phase was found to increase with ion fluence for $\theta = 0°$, whereas it remained almost constant for $\theta = 60°$.

Although the presence of a native oxide layer was detected in the pristine sample, the same would get quickly sputtered away during irradiation, considering the sputtering yield of ~3.4 of InSb for normally incident 60 keV Ar$^+$-ions (obtained from TRIDYN simulation[32]). In fact, corresponding to this sputtering yield, even the lowest fluence of 10^{17} ions cm^{-2} would amount to a sputtered layer thickness of ~100 nm, which is orders of magnitude higher than the native oxide layer thickness on the pristine InSb. In addition, the vacuum during irradiation was 5×10^{-7} mbar, which

TABLE I. Composition of pristine and irradiated InSb surfaces as extracted from XPS.

B.E. (eV) / Fluence (ions cm^{-2})	In in InSb 444.3/451.8	In in In_2O_3 445.2/452.7	Sb in InSb 527.4/536.8	Sb in Sb_2O_3 530.2/539.7	O 1*s* 531
Pristine	53.5	56.5	7.8	28.8	63.4
1×10^{17}; $\theta = 0°$	29.7	70.3	6.5	24.6	68.9
3×10^{18}; $\theta = 0°$	56.1	43.9	1.8	32.3	65.9
1×10^{17}; $\theta = 60°$	60.9	39.1	7.2	26.5	66.3
3×10^{18}; $\theta = 60°$	56.6	43.4	4.8	26.2	69

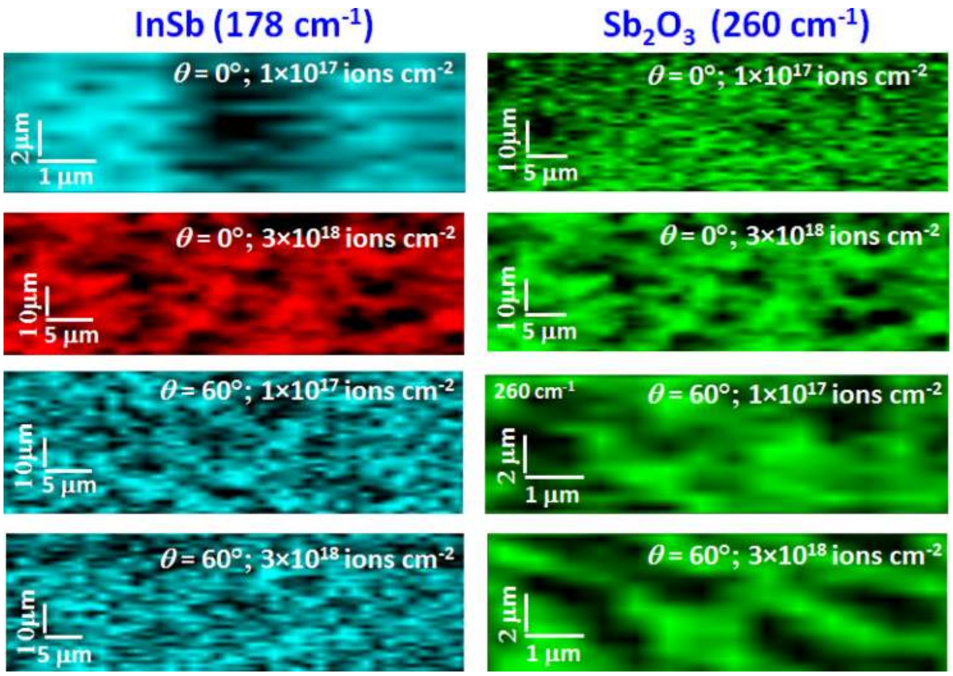

FIG. 6. Raman mapping data of InSb and Sb_2O_3 taken over the Ar^+-ion irradiated porous structures. Angle of ion incidence and ion fluence are shown on the images.

would not lead to any oxidation of the samples even after the irradiation got completed. Evidently, the observed oxidation of the porous microstructures occurred upon exposing the irradiated samples to the ambient.

It may be mentioned that although the presence of oxide phases in the ion-generated structures was established by the results from Raman spectroscopy and XPS, the question of the spatial distribution of the chemical phases such as Sb_2O_3 over the surface remained open. In order to find out the spatial distribution of the chemical phases, we carried out Raman mapping of irradiated InSb samples. The Raman peaks selected for the mapping were $178\,cm^{-1}$ corresponding to TO mode of InSb and $260\,cm^{-1}$ corresponding to Sb_2O_3. The Raman maps are shown in Figs. 6(a)–6(d) for InSb and in Figs. 6(e)–6(h) for Sb_2O_3 as a function of ion fluence and angle of incidence. The corresponding morphology of the irradiated InSb can be followed from SEM images of Figs. 1(a) and 1(c) for $\theta = 0°$ and from Figs. 2(a) and 2(c) for $\theta = 60°$, respectively. A comparison of Raman mapping images of InSb and Sb_2O_3 for $\theta = 0°$ to the lowest and the highest ion fluences with corresponding SEM images makes it clear that Sb_2O_3 was present all over the porous microstructures formed due to normally incident ions. On the other hand, Raman mapping of Sb_2O_3 on the sample irradiated to the highest fluence at $\theta = 60°$ showed strips, whereas the InSb signal was distributed all over the implanted surface. A comparison with SEM images made it evident that the Sb_2O_3 signal was coming from the strips of porous structures. In other words, oxidation was higher on the porous microstructures in comparison to the bare surface observed in between the strips.

To further explore the crystallinity aspect of ion-induced nanoporous structures at the high fluence regime of the present study, we performed GIXRD studies. The GIXRD spectra (Fig. 7) of the samples irradiated at $\theta = 0°$ showed peaks at $2\theta = 24°$, 39.1°, and 45.4°, respectively. These peaks were assigned to (111), (220), and (311) peaks of a cubic InSb structure.[33] The GIXRD spectra from the samples irradiated at $\theta = 60°$ showed similar peaks (not shown). The peaks observed in the GIXRD spectra clearly indicated that nanocrystallites were present in the porous microstructure even after irradiation to the highest fluence. Using the full width at half maximum (FWHM) of the (111) diffraction peak in the Scherrer's formula,[34] the average crystallite size turned out to be around 3 nm and 4 nm for $\theta = 0°$ and 60°, respectively.

Since the presence of crystallites was detected up to the highest applied fluences, these two samples were investigated by XTEM. An XTEM micrograph of the sample corresponding to $\theta = 0°$ is shown in Fig. 8(a). The interconnected

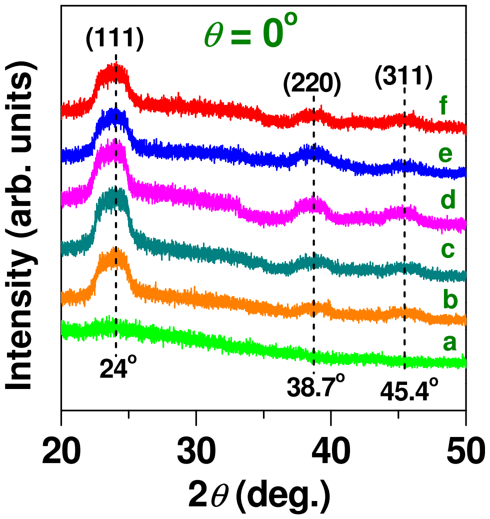

FIG. 7. GIXRD spectra of InSb samples irradiated at $\theta = 0°$ to fluences of (a) pristine InSb, (b) 1×10^{17} ions cm^{-2}, (c) 4×10^{17} ions cm^{-2}, (d) 7×10^{17} ions cm^{-2}, (e) 1×10^{18} ions cm^{-2}, and (f) 3×10^{18} ions cm^{-2}. The spectra are shifted along the y-axis for better clarity.

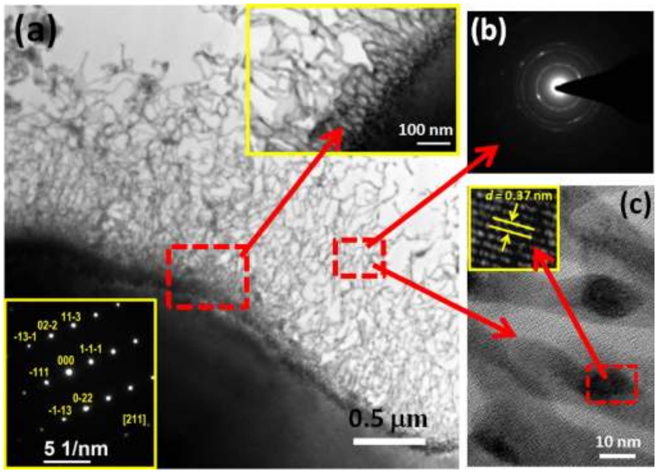

FIG. 8. (a) XTEM image of InSb sample irradiated to fluence of 3×10^{18} ions cm^{-2} at $\theta = 0°$. The inset at the top right corner of (a) shows a magnified view of the interface region of the porous layer with the substrate underneath. The inset at the bottom left corner of (a) shows the SAED pattern obtained from the substrate. The SAED pattern obtained from the nanofibrous layer is shown in (b). HRTEM image of nanofibers in (c) shows the nanocrystallites embedded in amorphous matrix where the inset demonstrates lattice fringes arising from the nanocrystallites.

network of ion-induced nanofibers was clearly observed from the same. The widths of the Nanofibers, measured from XTEM micrographs, were in the range of 10–25 nm and agreed well with the results obtained from XSEM study. The inset in the top right corner of Fig. 8(a) presents a magnified view of the interface region of the nanofibrous layer with the substrate underneath, showing the voids and plate-like structures in this region. The inset in the bottom left corner of Fig. 8(a) depicts the selected area electron diffraction (SAED) pattern obtained from the substrate underneath where ordered diffraction spots, corresponding to an fcc lattice along the $[1\bar{1}\bar{2}]$ direction, were seen, exhibiting the single-crystalline nature of the substrate. On the other hand, the SAED pattern shown in Fig. 8(b), collected from the nanofibrous layer [shown in Fig. 8(a)], would indicate a textured pattern consisting of bright spots over concentric rings, which were indicative of oriented InSb crystallites within the nanofibers. The presence of nanoscale crystallites embedded in the amorphous matrix also became obvious from the high-resolution TEM (HRTEM) image shown in Fig. 8(c) where lattice fringes were observed from the nanocrystallites embedded in the amorphous matrix. The *d*-spacing measured from the lattice fringes turned out to be 0.37 nm and matched with the d_{111} of cubic zinc-blend structure of InSb, This corroborates well with the GIXRD data described above.

The XTEM image of InSb irradiated to 3×10^{18} ions cm^{-2} at $\theta = 60°$ is shown in Fig. 9(a). The XTEM image revealed the presence of large voids (~100 nm) in the ion-induced porous layer, in contrast to nanofibers observed for $\theta = 0°$. A comparison with the corresponding XSEM image in Fig. 2(d) suggests that the large voids were the cavities enclosed by the plate-like structures. In Figs. 9(b) and 9(c), we have shown two SAED patterns obtained from the regions marked as "1" and "2" [enclosed by the red circles in Fig. 9(a)]. The SAED pattern in Fig. 9(b) (from the top region of the porous layer) demonstrated that the specimen got textured about a direction at an angle to the beam, so the Ewald sphere created elongated spots or arcs in the diffraction pattern. On the other hand, the SAED pattern from the bottom part of the porous layer in Fig. 9(c) is indicative of relatively more textured nature. This is an important observation as in this way oriented crystalline nanowires can be formed. The HRTEM image in Fig. 9(d), obtained from the top part of the porous layer, showed highly damaged and partially amorphous structure, which is consistent with the SAED pattern in Fig. 9(b). The *d*-spacing, measured from the lattice fringes seen in the HRTEM image [Fig. 9(e)], was measured to be 0.37 nm, which matched with d_{111} of cubic

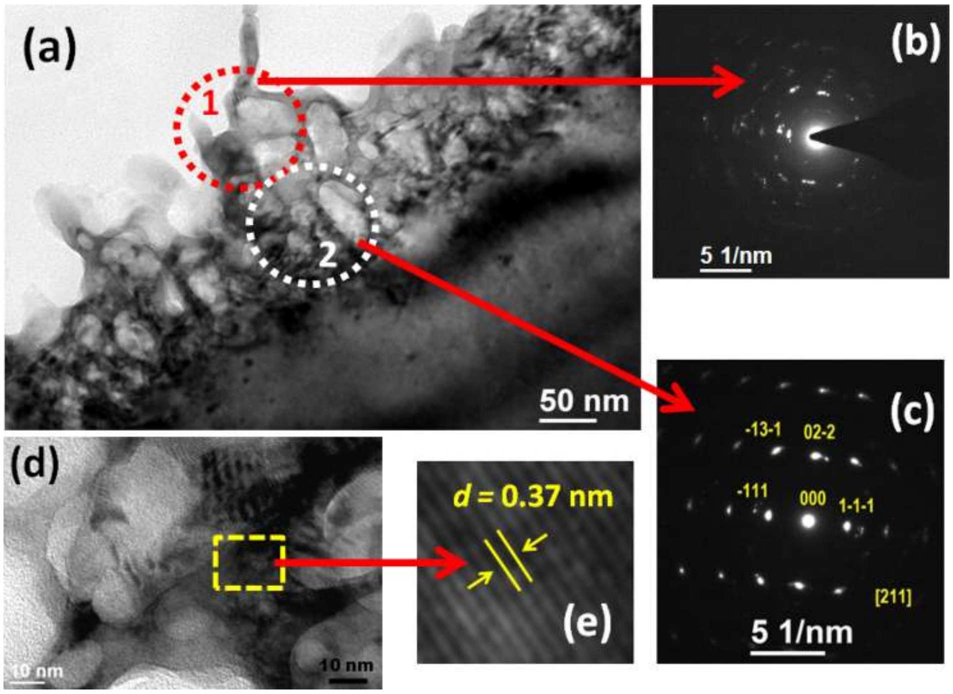

FIG. 9. (a) XTEM image of InSb sample irradiated to the fluence of 3×10^{18} ions cm^{-2} at $\theta = 60°$. SAED patterns obtained from the regions marked "1" and "2" in (a) are shown in (b) and (c), respectively. Ion-damaged structure of the porous layer is shown in the HRTEM image in (d). The *d*-spacing of lattice fringes observed in (d) is shown in (e).

zinc-blend structure of InSb (similar to the one obtained from the porous layer generated by normally incident ions).

We now attempt to understand the observed modifications of InSb in light of basic ion-solid interactions. Earlier studies involving MeV energy ions[11–13] attributed the formation of porous structure to a mechanism similar to the one invoked for GaSb.[17,18] Nuclear energy loss of incident ions inside the target matrix resulted in formation of defects, i.e., vacancies and interstitials. Owing to the inefficient recombination of interstitials with vacancies, vacancy concentration in the target matrix increased with ion irradiation, which finally led to accumulation of vacancies into voids. This process is schematically represented in Figs. 10(a) and 10(b) for normally incident ion irradiation. Fig. 10(a) shows the initial stage of irradiation where the vacancies and interstitials were produced up to a depth of the order of projected range of ions, whereas Fig. 10(b) depicts the situation when voids were formed by vacancy aggregation. Subsequent to void formation, ions did lose energy only in the "thin walls" in between the voids [indicated in Fig. 10(b)], while no energy loss took place for ion-paths within the voids. As a result, ions penetrated deeper into the matrix beneath the void layer where further void nucleation took place. This mechanism led to void formation deeper and deeper in the target matrix, increasing the thickness of the void layer much higher than the projected range of ions.

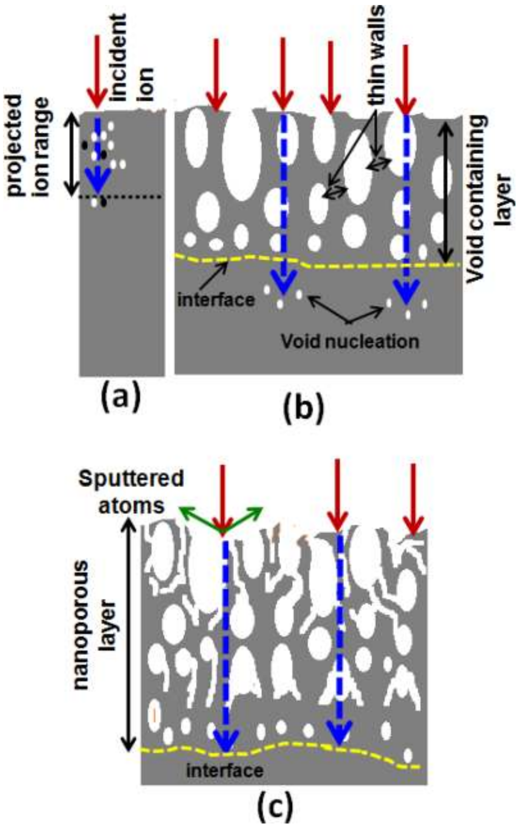

FIG. 10. Schematic representation of the processes leading to the formation of nanoporous layer in InSb. The white and black dots in (a) depict vacancies and interstitials created along the ion path up to the projected range. The dashed blue arrows represent the ion path inside InSb. The green arrows depict atoms sputtered from the surface. The dotted yellow line on the diagrams (b) and (c) denote the interface of nanoporous layer and the underlying InSb substrate.

According to the mechanism described above, the void dimension at a certain depth was proportional to the rate of vacancy generation. Primarily, voids were formed within a layer that extended up to the projected range. Subsequent to their formation, a few vacancies were generated within the thin walls separating the voids by incident ions penetrating deeper into the substrate [Fig. 10(b)]. These vacancies migrated to the existing voids leading to an increase in the void dimension, while smaller voids nucleated in the substrate underneath. Thus, the dimensions of the voids became a function of depth where voids of smallest dimension were expected to form at a depth up to which the ions reached after losing their energy. On the other hand, as the voids grew with irradiation, they started to coalesce with each other, leading to the gradual formation of a porous layer of interconnected nanofibers [Fig. 10(c)]. This schematic picture provides a qualitative explanation of our experimentally observed nanofibrous network formation under normally incident ion irradiation. The layer of small voids was seen at the interface of porous layer with the substrate underneath because ions reached at this depth after spending most of their energy in the porous layer above. Small voids were formed out of the few vacancies created by a small amount of energy deposited at this depth. In comparison, energy deposition and related vacancy generation were slightly higher in the region above the void layer, leading to an increase in void dimensions and partial coalescence. The columnar structures observed over the void layer, thus, could be correlated with the void walls remaining after partial void coalescence.

The presence of crystalline phases in the present experiment was also consistent with this qualitative understanding of evolution of a porous structure/network. Although our experimental studies were in the high fluence regime, comparison with earlier studies[11,13] suggests that the nanoporous structure got formed at much lower fluences, before transition of the crystalline InSb to a completely amorphous one. As a result, the "thin walls" separating the voids contained crystallites/highly damaged zones within the amorphized matrix. Since the dimension of the nanostructures observed in this fluence regime was very small ($\sim$10–25 nm), very small amount of energy deposited by the ions within the nanostructures could not produce radiation damage sufficient for conversion of the nanocrystallites to amorphous structure. Therefore, some crystallites remained embedded within the amorphous matrix.

In case of oblique incidence of ions, our study revealed the formation of plate-like structures up to the highest fluence used, viz. 3×10^{18} ions cm^{-2}. The thickness of the porous layer was observed to be much lower than that corresponding to normal irradiation. It may be noted that the projected range of ions for $\theta = 60^\circ$ is half of that for $\theta = 0^\circ$. As described above, initially void formation and their growth took place within a layer of thickness of the order of projected range. Thus, although the basic mechanism for porous layer development was similar to the case of normal ion incidence, the void layer thickness would be almost half for 60° incidence. For further irradiation, although thickness of the void-containing layer increased by ion-penetration into the bulk underneath, thickness of the layer remained lower than that for $\theta = 0^\circ$ for any oblique ion incidence. If we would take into account the randomness of ion penetration through voids in the fluence range under consideration, the lower thickness of the porous layer observed for ion incidence at $\theta = 60^\circ$ would be consistent with the qualitative understanding invoked here. Further, from simulation using Monte Carlo program SRIM-2012,[35] the vacancy generation rate in the surface layer of InSb for $\theta = 60^\circ$ was found to be higher than for $\theta = 0^\circ$. As a result, the void growth rate was higher for $\theta = 60^\circ$ than that for $\theta = 0^\circ$. It may be noted that in XSEM images [Figs. 2(b) and 2(d)], we observed large cavities enclosed by the plate-like structures. This type of microstructure seemed to be caused by high growth rate of voids at oblique ion incidence. However, the question as to why the plate-like structure did not transform into a nanofibrous network remains beyond the scope of the present qualitative model.

It should be mentioned that recently we observed formation of a rough top layer during development of porous layer by obliquely incident (for $\theta = 60^\circ$) 60 keV Ar^+-ion irradiation of GaSb.[17] The observed result was explained by considering the effect of redeposition of sputtered atoms on top of the porous layer during ion irradiation. Competition of redeposition of sputtered atoms with vacancy mediated porous structure formation resulted in the formation of a top layer. However, such structural modification was not observed for ion irradiation of InSb at $\theta = 60^\circ$. The reason could be possibly the considerable higher rate of vacancy generation in InSb compared to GaSb. For the present experimental condition, SRIM-2012 simulation yielded the number of vacancy generated per incident ion to be 1818 in InSb (with an average uncertainty of 7.5%), which was almost double than that of 968 for GaSb and thus, the growth rate of porous structure was almost two times faster in InSb compared to GaSb. As a result, the porosity development dominated over redeposition and the porous layer remained exposed up to the highest applied fluence of the present study.

The high degree of oxidation of the porous layer seems to be due to the reactive natures of In and Sb. Indeed, high level of oxidation of InSb surface was detected in earlier experimental studies, which was attributed to the reactive natures of In and Sb, leading to the formation of oxide phases on the surface layer.[27–30] The oxidation process of InSb could be understood by the following reaction:[27]

$$2\mathrm{InSb} + 3\mathrm{O_2} = \mathrm{In_2O_3} + \mathrm{Sb_2O_3}. \tag{1}$$

Since Sb_2O_3 is metastable in nature while it is in contact with InSb, the following reaction would take place:

$$\mathrm{Sb_2O_3} + 2\mathrm{InSb} = \mathrm{In_2O_3} + 4\mathrm{Sb}. \tag{2}$$

In fact, accumulation of a group V element at the interface of oxide and III–V semiconductor interface is well known.[27] Thus, the elemental Sb created through the above reaction (Eq. (2)) could be assumed to have accumulated at the interface of In_2O_3 and InSb. We note that elemental Sb signal was detected in the micro-Raman spectra of all irradiated InSb samples [Figs. 4(a) and 4(b)]. The above reaction showed the origin of this elemental Sb in the porous microstructures.

Since the oxidation takes place due to exposure of the porous structures to ambient, the extent of oxidation should be proportional to the effective surface area. The experimentally observed O concentration (Table I) is highly consistent with this. For $\theta = 0^\circ$, the amount of oxygen (at the lowest fluence) corresponded to the microstructures shown in Figs. 1(a) and 1(b), where some plate-like structures were seen at the interface of the porous layer with the substrate underneath. When the ion fluence increased, the thickness of the porous layer increased according to the mechanism discussed above. In other words, the surface area of the porous layer effectively increased. Thus, an increase in oxygen absorption was observed in the EDS spectra. For $\theta = 60^\circ$, plate-like structures evolved and the increment in the surface area was not sufficient to give rise to appreciable change in O concentration detectable by EDS.

A question arises regarding the porous microstructures observed in the present case, which was in contrast to the formation of ripple patterns or cone-like structures during FIB irradiation.[12,15,16] We note that FIB irradiations in the earlier studies were performed over a small area of a few micron. With this small area and considering the high ion flux used in those studies, there will be considerable increase in temperature during irradiation. As a result, the recombination rate of vacancies and interstitials might be significantly higher than the present case where ion irradiation was carried out over an area $\sim 1\ \mathrm{cm}^2$. Thus, the effect of sputtering would be higher than the vacancy-mediated void formation, leading to cone-like structure instead of a porous microstructure.

IV. CONCLUSIONS

In summary, we showed the evolution of porous microstructure during medium energy Ar^+-ion irradiation of InSb in the high fluence regime. Our study demonstrated that while a network of nanofibers evolved under normally incident ions, plate-like structures were generated under oblique ion incidence of 60°. We further showed that evolution of porous structures can be qualitatively understood in terms of defect accumulation due to ion irradiation and subsequent void growth. The structural difference observed for oblique ion incidence was correlated to higher defect accumulation within a smaller volume. The present experimental results not only provided a route to fabricate nanofibers but also indicated significant difference from FIB processing. In addition, the present study demonstrated the existence of crystalline phase in the ion-generated nanostructures in the high fluence regime, which could have important implications for possible optical or optoelectronics application of the nanofibers since the dimension of the observed structures was well below the Bohr radius of excitons in InSb. Experimental investigations on the optical properties of these nanostructures are under way. Moreover, we detected high degree of oxidation of the nanostructures (with the presence of In_2O_3 and Sb_2O_3 phases) subsequent to an exposure of the samples to ambient. The oxide phases on the nanostructures could make them useful in sensors or in catalytic devices.[36,37]

ACKNOWLEDGMENTS

The authors gratefully acknowledge helps received from Professor Shikha Varma, Institute of Physics, Bhubaneswar for XPS studies, and Pravakar Mallick, National Institute of Science Education and Research, Bhubaneswar for SEM measurements. The authors would also like to acknowledge technical help received from Dr. Sriparna Chatterjee, Institute of Minerals and Materials Technology, Bhubaneswar during this study.

[1] Z. Zhao, K. Yadavalli, Z. Hao, and K. L. Wang, Nanotechnology **20**, 035304 (2009).

[2] B. R. Bennett, R. Magno, J. B. Boos, W. Kruppa, and M. G. Ancona, Solid State Electron. **49**, 1875 (2005).

[3] P. S. Dutta, H. L. Bhat, and V. Kumar, J. Appl. Phys. **81**, 5821 (1997).

[4] S. Mokkapati and C. Jagadish, Mater. Today **12**, 22 (2009).

[5] A. T. Vogel, J. de Boor, J. V. Wittemann, S. L. Mensah, P. Werner, and V. Schmidt, Cryst. Growth Des. **11**, 1896 (2011).

[6] X. Cai and J. Wei, J. Appl. Phys. **114**, 083507 (2013).

[7] S. R. Das, C. J. Delker, D. Zakharov, Y. P. Chen, T. D. Sands, and D. B. Janes, Appl. Phys. Lett. **98**, 243504 (2011).

[8] R. K. Paul, S. Badhulika, and A. Mulchandan, Appl. Phys. Lett. **99**, 033103 (2011).

[9] X. Zhang, Y. Hao, G. Meng, and L. Zhang, J. Electrochem. Soc. **152**, C664 (2005).

[10] C. Pendyala, S. Vaddiraju, J. H. Kim, J. Jacinski, Z. Chen, and M. K. Sunkara, Semicond. Sci. Technol. **25**, 024014 (2010).

[11] S. M. Kluth, D. Llewellyn, and M. C. Ridgway, Nucl. Instrum. Methods Phys. Res., Sect. B **242**, 640 (2006).

[12] A. G. Perez-Bergquist, K. Li, Y. Zhang, and L. Wang, Nanotechnology **21**, 325602 (2010).

[13] N. Nitta, T. Hasegawaa, H. Yasudaa, K. Satob, M. Taniwakic, and A. Hatta, Radiat. Eff. Defects Solids **168**, 247 (2013).

[14] H. Simchi, M. Raastgoo, A. Ranjbar, T. Barzekar, M. Qasempour, M. Daaraei, E. Mahmoodzadeh, M. H. Saani, and Sh. Mohammadnejad, Infrared Phys. Technol. **52**, 113 (2009).

[15] J. H. Wu and R. S. Goldman, Appl. Phys. Lett. **100**, 053103 (2012).

[16] M. Kang, J. H. Wu, W. Ye, Y. Jiang, E. A. Robb, C. Chen, and R. S. Goldman, Appl. Phys. Lett. **104**, 052103 (2014).

[17] D. P. Datta, A. Kanjilal, S. K. Garg, P. K. Sahoo, D. Kanjilal, and T. Som, J. Appl. Phys. **115**, 123515 (2014).

[18] D. P. Datta, A. Kanjilal, S. K. Garg, P. K. Sahoo, B. Satpati, D. Kanjilal, and T. Som, Appl. Surf. Sci. **310**, 189 (2014).

[19] T. Dhawan, A. G. Vedeshwar, V. N. Singh, B. R. Mehta, and R. P. Tandon, Scr. Mater. **63**, 97 (2010).

[20] B. S. Naidu, M. Pandey, V. Sudarsan, R. K. Vatsa, and R. Tewari, Chem. Phys. Lett. **474**, 180 (2009).

[21] K. Ersching, C. E. M. Campos, J. C. de Lima, T. A. Grandi, S. M. Souza, and P. S. Pizani, Mater. Chem. Phys. **122**, 528 (2010).

[22] M. Yin and A. Krier, Infrared Phys. Technol. **58**, 47 (2013).

[23] C. Seok, M. Choi, S. Park, J. Jung, Y. Park, I. Yang, and E. Yoon, ECS Sol. Stat. Lett. **3**, 27 (2014).

[24] X. Zhou, W. Guo, A. G. Perez-Bergquist, Q. Wei, Y. Chen, K. Sun, and L. Wang, Nanoscale Res. Lett. **6**, 6 (2011).

[25] S. G. Kim, H. Asahi, M. Seta, J. Takijawa, S. Emura, R. K. Soni, and S. Gonda, J. Appl. Phys. **74**, 579 (1993).

[26] J. H. Dias da Silva, S. W. da Silva, and J. W. Galzerani, J. Appl. Phys. **77**, 4044 (1995).

[27] O. E. Tereshchenko, Appl. Surf. Sci. **252**, 7684 (2006).

[28] W. K. Liu and M. B. Santos, J. Vac. Sci. Technol., B **14**, 647 (1996).

[29] R. J. Iwanowski, M. H. Heinonen, J. Raczyńska, and K. Fronc, Appl. Surf. Sci. **153**, 193 (2000).

[30] D. Aureau, R. Chaghi, I. Gerard, H. Sik, J. Fleury, and A. Etxheberry, Appl. Surf. Sci. **276**, 182 (2013).

[31] J. Lee, S. Park, J. Kim, C. Yang, S. Kim, C. Seok, J. Park, and E. Yoon, Thin Solid Films **520**, 5382 (2012).

[32] W. Möller and W. Eckstein, Nucl. Instrum. Methods Phys. Res., Sect. B **2**, 814 (1984).

[33] X-Ray diffraction database, JCPDS-International Centre for Diffraction Data, 73-1985 (1998).

[34] A. L. Patterson, Phys. Rev. **56**, 978 (1939).

[35] J. Ziegler, J. P. Biersack, and M. D. Ziegler, *SRIM—The Stopping and Ranges of Ions in Solids* (SRIM Co., Chester, 2008); See www.srim.org/ for SRIM—The Stopping and Ranges of Ions in Solids.

[36] S. Yi, S. Tian, D. Zeng, K. Xu, S. Zhang, and C. Xie, Sens. Actuators, B **185**, 345 (2013).

[37] H. W. Kim, H. Sung Kim, H. G. Na, J. C. Yang, M. A. Kebede, and C. Lee, Ceram. Int. **37**, 593 (2011).